American Journal of Analytical Chemistry, 2017, 8, 523-539
http://www.scirp.org/journal/ajac
ISSN Online: 2156-8278
ISSN Print: 2156-8251

A New Insight in the Physical and Photoelectrochemical Properties of Molybdenum Disulfide Alpha-Hematite Nanocomposite Films

Hussein Alrobei[1], Ashok Kumar[1], Manoj K. Ram[2]

[1]Department of Mechanical Engineering, University of South Florida, Tampa, FL, USA
[2]Clean Energy Research Center, University of South Florida, Tampa, FL, USA
Email: mkram@usf.edu; manojkram@gmail.com

How to cite this paper: Alrobei, H., Kumar, A. and Ram, M.K. (2017) A New Insight in the Physical and Photoelectrochemical Properties of Molybdenum Disulfide Alpha-Hematite Nanocomposite Films. *American Journal of Analytical Chemistry*, **8**, 523-539.
https://doi.org/10.4236/ajac.2017.88038

Received: July 20, 2017
Accepted: August 28, 2017
Published: August 31, 2017

Abstract

The alpha (α)-hematite (Fe_2O_3) as photoanode has been used for photoelectrochemical applications due to low bandgap, low cost, high chemical stability, nontoxicity, and abundance in nature. The doping with various transition metals, formation of nanostructured and nanocomposite of α-Fe_2O_3 have been attempted to enrich the carrier mobility, surface kinetics and carrier diffusion properties. The manuscript is an attempt to improve the photoelectrochemical properties of α-Fe_2O_3 by formation of nanocomposite with dichalcogenide (molybdenum disulfide (MoS_2) nanomaterials. The nanocomposite of MoS_2-α-Fe_2O_3 have been synthesized by varying the amount of MoS_2 in sol-gel synthesis process. The nanocomposite MoS_2-α-Fe_2O_3 materials were characterized using UV-visible, FTIR, SEM, X-ray diffraction, Raman and particle analyzer. The photoelectrochemical properties were investigated using cyclic voltammetry and chronoamperometry studies. The optical and structural properties of MoS_2-α-Fe_2O_3 nanocomposite have been found to be dependent on MoS_2 doping. The band gap has shifted whereas; the structure is more prominent as flower-like morphology, which is a result of doping of MoS_2. The photocurrent is more pronounced with and without light exposition to MoS_2-α-Fe_2O_3 based electrode in photoelectrochemical cell. We have understood the photoelectrochemical water splitting using nanocomposite α-Fe_2O_3-MoS_2 through schematic representation based on experimental results. The enhanced photoelectrochemical properties of nanocomposite α-Fe_2O_3-MoS_2 films have been observed as compared to pristine α-Fe_2O_3 and transition metal doped α-Fe_2O_3 nanostructured films.

Keywords

Water Splitting, Photoelectrochemical, Hematite (α-Fe_2O_3), MoS_2, Nanocomposite

1. Introduction

Photoelectrochemical cell (PEC) produces hydrogen through splitting the water using renewable sources (*i.e.*, the sun) [1] [2] [3]. Photoelectrochemical (PEC) cells have been used to convert solar energy to hydrogen gas by splitting water into hydrogen and oxygen, hence offering clean and renewable energy [4]. Moreover, photoelectrochemical (PEC) has attracted attention since Honda and Fujishima utilized the first application of titanium dioxide (TiO_2) in 1972 [5]. Nevertheless, the large bandgap of TiO_2 (3.1 - 3.3 eV) impedes the absorption of visible light, and limits the solar-to-hydrogen efficiency to 2.2% [5]. So, it is necessary to use material that has small bandgap and easy to harvest energy from sunlight (visible light 53%) [6]. Iron oxide, bismuth vanadate, tungsten oxide, and tantalum nitride are the examples of low band gap semiconducting materials [5]. The α-Fe_2O_3 is one of the most attractive photo-anode materials with efficiency of 16% to convert solar-to-hydrogen [5] [7]-[14]. The α-Fe_2O_3 has been applied for photoelectrochemical applications due to low bandgap (2.1 - 2.2 eV), low cost, high chemical stability, nontoxicity, and abundance in nature [5]. However, α-Fe_2O_3 also has several drawbacks such as shorter hole diffusion length, low conductivity, shorter life time of photoexcitation and deprived reaction kinetics of oxygen evolution in photoelectrochemical applications [15]. The doping with several metallic ions such as zinc [16], titanium [17] [18], molybdenum [19], aluminum [20], platinum [21], silicon [22] [23] [24], graphene [25] [26], and cadmium sulfide [27] have shown improved PEC performance. The zinc and aluminum doped α-Fe_2O_3 have shown enhanced photoelectrochemical properties compared to α-Fe_2O_3 nanostructures [28] [29] [30].

Recently, two-dimensional (2D) dichalcogenide material "molybdenum disulfide (MoS_2)" with bandgap of 1.8 eV has been used as n-and p-types structures for photoelectrochemical studies [5]. The MoS_2 shows stimulating photocatalytic activity due to its bonding, chemical composition, doping, and nanoparticles growth on various film matrices, and has been used for hydrogen production in nanocluster structures [2] [31] [32] [33] [34]. Besides, MoS_2 has shown different applications in photocatalyst, phototransistors and sensors applications [5]. It is understood that MoS_2 could help to play an important role as the charge transfer with slow recombination of electron-hole pairs created due to photoenergy with the charge transfer rate between surface and electrons [35].

Under this work, MoS_2 particles were used to promote electron transport properties of the α-Fe_2O_3 nanomaterial by doping and homogenous structure due to MoS_2-α-Fe_2O_3 nanomaterials. The doping of MoS_2 particles varied by

0.1%, 0.2%, 0.5%, 1%, 2% and 5% in α-Fe_2O_3. The MoS_2-α-Fe_2O_3 nanomaterials were characterized using X-ray diffraction, SEM, FTIR, Raman spectroscopy, particle analyzer, and UV-vis techniques. The cyclic voltammetry (CV) and impedance measurements were utilized to understand the electrochemical electrode/electrolyte interface and photoelectrochemical properties of MoS_2-α-Fe_2O_3 based nanostructures for water splitting applications.

2. Experimental Details

2.1. Materials

The materials iron chloride ($FeCl_3$), aluminum chloride ($AlCl_3$), sodium hydroxide (NaOH), MoS_2, and ammonium hydroxide (NH_4OH) were purchased from Sigma-Aldrich. The fluorine tin oxide (FTO) coated glass with resistance of ~10 Ω was also procured from Sigma-Aldrich. The centrifuged containers were purchased to clean the synthesized nanomaterials from the solution.

2.2. Experimental Procedure

α-Fe_2O_3 and MoS_2-α-Fe_2O_3 were synthesized by a sol-gel technique as shown in Equation (1).

$$FeCl_3 \cdot 6H_2O + MoS_2 \xrightarrow[\text{NaOH (heat 110°C)/sonination/dry/heat}]{} MoS_2\text{-}Fe_2O_3 \quad (1)$$

Table 1 shows the amount of chemicals used for the synthesis of MoS_2-α-Fe_2O_3. Different concentrations of $FeCl_3$ with MoS_2 were prepared in 500 ml round bottom flasks. NaOH solution was added to the resulting solution and stirred with a magnet for an hour. A condenser was connected to the round bottom flask, which allowed chemical reaction to proceed at 90˚C - 100˚C. The reaction was terminated after 24 hours, and the solution was cooled at room temperature. The synthesized material was separated using a centrifuge and continuous cleaning with water and initially left drying in room temperature. The synthesized materials containing different ratios of α-Fe_2O_3 to MoS_2 in MoS_2-α-Fe_2O_3 were obtained. Figure 1 shows the photographs of the MoS_2-α-Fe_2O_3 materials synthesized using various percentage of MoS_2 to α-Fe_2O_3. The immediate doping of 0.1% MoS_2 changes the color of α-Fe_2O_3, whereas the dark red color can be visualized with the increase of MoS_2 percentage in α-Fe_2O_3. The MoS_2-α-Fe_2O_3 at various ratio were dried at various temperatures (100˚C, 200˚C, 300˚C, 400˚C,

Table 1. The amount of chemical used for synthesis of MoS_2-composite α-hematite.

Chemicals	0.1% MoS_2 w.r. to $FeCl_3$	0.2% MoS_2 w.r. to $FeCl_3$	0.5% MoS_2 w.r. to $FeCl_3$	1% MoS_2 w.r. to $FeCl_3$	2% MoS_2 w.r. to $FeCl_3$	5% MoS_2 w.r. to $FeCl_3$
$FeCl_3$	6.8 g	6.8 g	6.8 g	6.8 g	6.8 g	6.8 g
MoS_2	0.013 g	0.026 g	0.065 g	0.1296 g	0.2592 g	0.648 g
NaOH	4.8 g	4.8 g	4.8 g	4.8 g	4.8 g	4.8 g
$C_{19}H_{42}BrN$	0.5 g	0.5 g	0.5 g	0.5 g	0.5 g	0.5 g

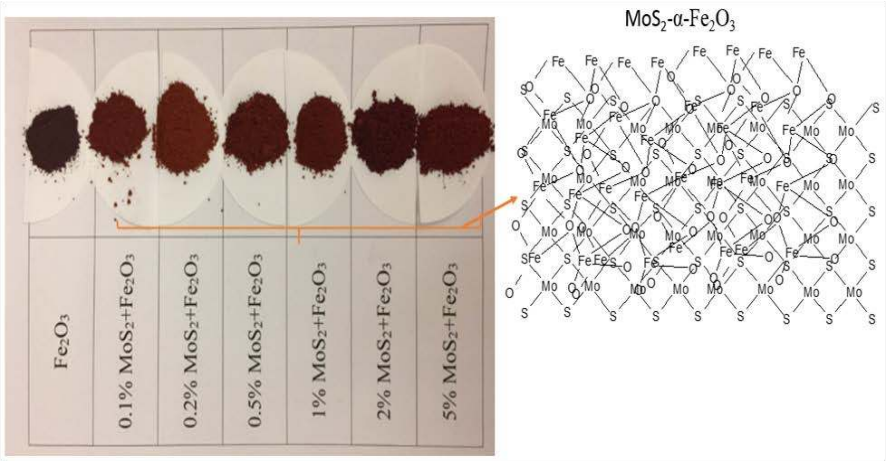

Figure 1. The synthesized α-hematite (α-Fe_2O_3) and MoS_2-α-Fe_2O_3 composite materials.

and 500˚C). In each case, the temperature was maintained in furnace for one hour. The materials were collected by cooling at room temperature and stored in a tight bottle for characterization as well preparation of electrodes for electrochemical and photochemical studies.

2.3. The Film Formation of Substrate

The MoS_2-α-Fe_2O_3 was prepared at different concentrations by mixing with acetic acid to obtain the homogenous solution to cast film on various substrates. 500 mg of MoS_2-α-Fe_2O_3 (0.1%, 0.2%, 0.5%, 1%, 2%, and 5%) was grinded and then mixed into 10 ml acetic acid in a container, and left for 10 hours. Later, homogenous colloidal solution containing MoS_2-α-Fe_2O_3 with acetic acid were used to make films on quartz, silicon, and fluorine tin oxide (FTO) coated glass plates. The films were cured at different temperatures (100˚C, 200˚C, 300˚C, 400˚C, and 500˚C) for an hour. It has been observed that the nanomaterials treated at 100˚C to 200˚C could still have the water molecules. However, the temperature at around 300˚C allowed to have a solid material. The nanomaterials were further treated to 400˚C and 500˚C. The XRD, SEM, cyclic voltammetry, and UV-vis characterizations were performed in room temperature in cooled samples which were heated till 500˚C of MoS_2-α-Fe_2O_3 films. We had observed passivation, change in structure and morphology in the samples treated at 300˚C, 400˚C and 500˚C. However, the results are presented for the samples treated at 500˚C due to their enhance photocurrent.

3. Results and Discussions

3.1. UV-Vis Studies

Figure 2 shows the UV-vis spectra of α-Fe_2O_3, MoS_2 and α-Fe_2O_3-MoS_2-prepared at a different ratio of MoS_2 to α-Fe_2O_3. An UV-Vis Spectrometer Jasco V-530 was used to measure the absorption spectra on various samples deposited on glass plates. **Figure 2(a)** shows the UV-vis absorption at around 550 nm for the

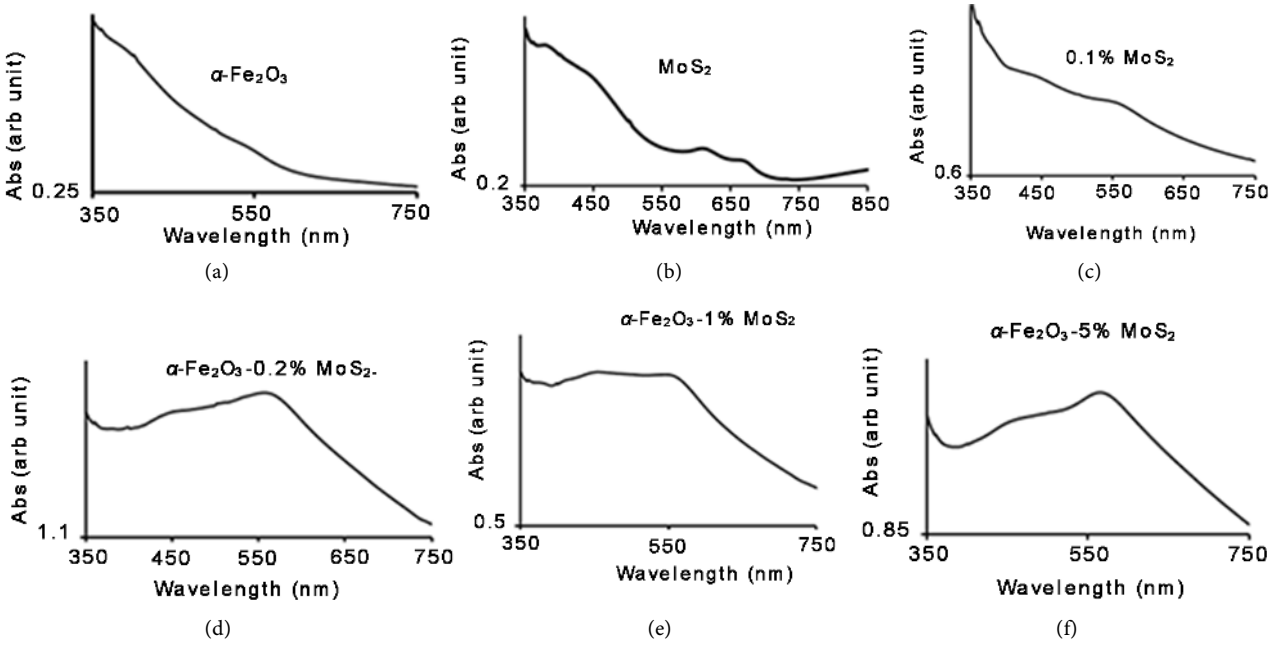

Figure 2. UV-vis absorption spectra of MoS_2 with α-hematite nanocomposite.

pristine α-Fe_2O_3 similar to shown in literature. **Figure 2(b)** shows the characteristics absorption bands 388, 453, 618 and 679 nm for the MoS_2 nanomaterial film on glass plates. **Figures 2(c)-(f)** shows the UV-vis absorption spectra for MoS_2 doped in different percentage (0.1%, 0.2%, 1% and 5%) with α-Fe_2O_3 nanomaterial. **Figure 2(c)** shows the absorption bands at 282, 454, 463 nm. **Figure 2(d)** shows the absorption bands at 446 and 565 nm. The distinct peaks can be seen at 382, 461 and 570 nm. **Figure 2(e)** absorbs the UV-vis band at 382, 456 and 559 nm whereas **Figure 2(f)** shows the absorption band at 382, 459 and 572 nm. There is a blue shift as an increase of MoS_2 in α-Fe_2O_3 [36]. However, the band observed for 0.1% MoS_2 doping is shifted at 572 nm in 5% MoS2 doping in α-Fe_2O_3 nanomaterial. Suchresults are consistent with the result shown of transition composite metal ions [37]. The UV-vis spectra of the composite hematite have been estimated to be 2.17 eV for the band at 572 nm.

3.2. XRD Studies

The crystalline structure of MoS_2-α-$Fe_2O_3$was investigated by using Powder X-ray diffraction (XRD), model PANalytical X'Pert Pro MRD system, with Cu K α radiation (wavelength = 1.5442 Å) operated at 40 kV and 40 mA. **Figure 3** shows X-ray diffraction curves for different percentage of MoS_2 (0.1%, 0.2%, 0.5%, 1%, 2%, and 5%) to α-Fe_2O_3; α-Fe_2O has polycrystalline structure as revealed from XRD pattern. The diffraction common peaks in MoS_2-α-Fe_2O_3 nanocomposite at different percentage of MoS_2 displays bands at 31.2˚, 33.2˚, 37.5˚, 40.9˚, 49.5˚, 54.1˚, 62.2˚, and 64.2˚ which can be indexed to (012), (104), (110), (113), (024), (116), (214), and (300) for crystal planes of hexagonal iron oxide [8]. It is clear from strong and sharp diffraction peaks that Fe_2O_3 is well crystallized

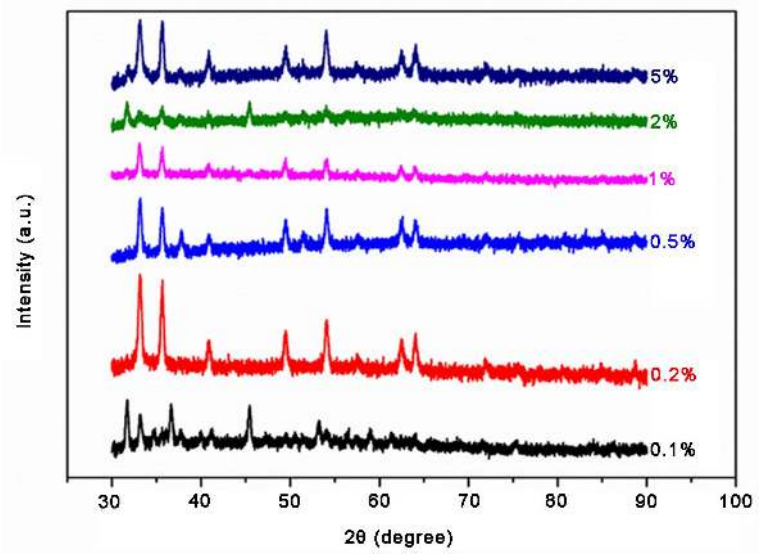

Figure 3. X-ray diffraction pattern of MoS_2 with α-hematite nanocomposite.

in the synthesis process for all percentage of MoS_2 in α-Fe_2O_3 [38]. The peak at 54.1˚ is due to the presence of MoS_2 in MoS_2-α-Fe_2O_3-structure.

3.3. FTIR Studies

Perkin Elmer spectrum one was utilized to study FTIR spectroscopy of various samples of MoS_2-α-Fe_2O_3-nanocomposite. The MoS_2-α-Fe_2O_3-nanocomposite was mixed with KBr, the pellets were made using the hydraulic press, and the samples were measured using the transmission mode from 400 to 4000 cm^{-1}. FTIR spectra of MoS_2-α-Fe_2O_3 shows the change of percentage of MoS_2 doping with α-Fe_2O_3 with Curve 1% to 5%, Curve 2% to 0.2%, Curve 3% to 2%, Curve 4 to 1%, Curve 5% to 0.5%, and Curve 6% to 0.1% of MoS_2 in MoS_2-α-Fe_2O_3 in shown in **Figure 4**. The infrared bands of each MoS_2 doping to α-Fe_2O_3 are shown in **Table 2**.

The hydroxyl (OH) groups in α-Fe_2O_3 is related to infrared band at 3414 cm^{-1}. The band at 1642 cm^{-1} is due to ν (OH) stretching. The band at 562 cm^{-1} is due to Fe-O vibration mode in Fe_2O_3. The band at 620 - 654 and 474 - 512 are related to the lattice defects in Fe_2O_3 [39] [40]. The infrared band at 474 - 512 cm^{-1} is due to stretching vibration depicting the presence of MoS_2 in the MoS_2-α-Fe_2O_3 structure. The doping of 0.1% to 5% of MoS_2 shifts the infrared band from 512 cm^{-1} to 474 cm^{-1}. The band at 474 cm^{-1} is the band observed for exfoliated MoS_2 nanosheets revealing that maximum doping in MoS_2-α-Fe_2O_3 structure [41].

3.4. SEM Studies

The scanning electron microscopy (SEM) of various MoS_2-α-Fe_2O_3 samples were measured using FE-SEM, S-800, Hitachi. **Figure 5** shows SEM images of MoS_2-α-Fe_2O_3 nanomaterials which consisted of different percentages from 0.1 to 5% MoS_2 to Fe_2O_3 in MoS_2-α-Fe_2O_3. SEM images reveals that the morphology

Table 2. The infrared bands of each MoS_2 doping to α-Fe_2O_3.

4. MoS_2	Wavenumber (cm^{-1})
5%	474, 562, 620, 1136, 1193, 1472, 1642, 2858, 2924, 3436
2%	484, 562, 620, 1136, 1193, 1472, 1642, 2858, 2924, 3436
1%	474, 570, 640, 1006, 1134, 1388, 1470, 1670, 2854, 2924, 3436
0.5%	458, 554, 644, 802, 898, 1042, 1386, 1468, 1634, 2856, 2922, 3438,
0.1%	512, 522, 654, 802, 1114, 1396, 1434, 1666, 2836, 2952, 3448

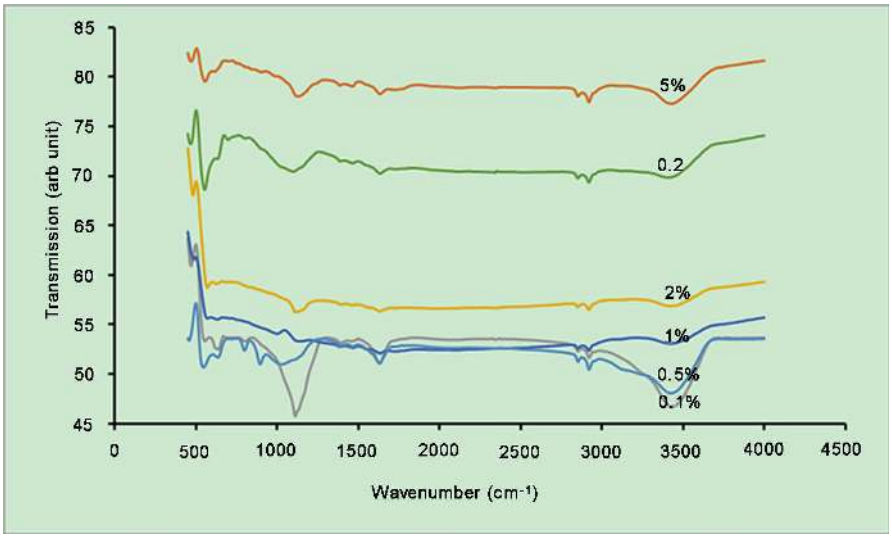

Figure 4. FTIR spectra of MoS_2 with α-hematite nanocomposite. Each curve MoS_2 doping with Fe_2O_3 is given as: Curve 1 = 5% MoS_2, Curve 2 = 0.2% MoS_2-Fe_2O_3, and Curve 3 = 2% MoS_2-Fe_2O_3, Curve 4 = 1% MoS_2-Fe_2O_3, Curve 5 = 0.5% MoS_2-Fe_2O_3 and Curve 6 = 0.1% MoS_2-Fe_2O_3.

MoS_2-α-Fe_2O_3 resembles blooming flower-like nanoparticles. The blooming flower-like morphology is a result of doping MoS_2 with α-Fe_2O_3 [42]. The images reveal that the size of the particle changes with the increase of MoS_2 doping from 0.1% to 5% in MoS_2-α-Fe_2O_3 nanomaterial. Besides, it is difficult to differentiate simple α-Fe_2O_3 nanoparticles from MoS_2 nanosheets; this shows a strong interface formation between Fe_2O_3 and MoS_2in MoS_2-α-Fe_2O_3 nanomaterial [43].

3.5. Raman Spectroscopy

The Raman spectrum is measured which is also a rapid and nondestructive surface characterization technique to probe the vibrational properties of bonding of MoS_2 to Fe_2O_3 in MoS_2-α-Fe_2O_3 nanomaterial. **Figure 6** shows the Raman spectra of MoS_2-α-Fe_2O_3 film excited by 532 nm laser [44]. The Raman shift at 532 cm^{-1} resonates with the electronic transition in ring structures for aromatic clustering processes in sp^2-dominated particles. The shift associated at 374 and 417 cm^{-1} are due to in-plane vibrational (E_{2g1}) and the out-of-plane vibrational (A_{1g}) modes. The enhanced MoS_2 is indicative of energy difference between Raman shifts due to MoS_2 content in MoS_2-α-Fe_2O_3 nanomaterial.

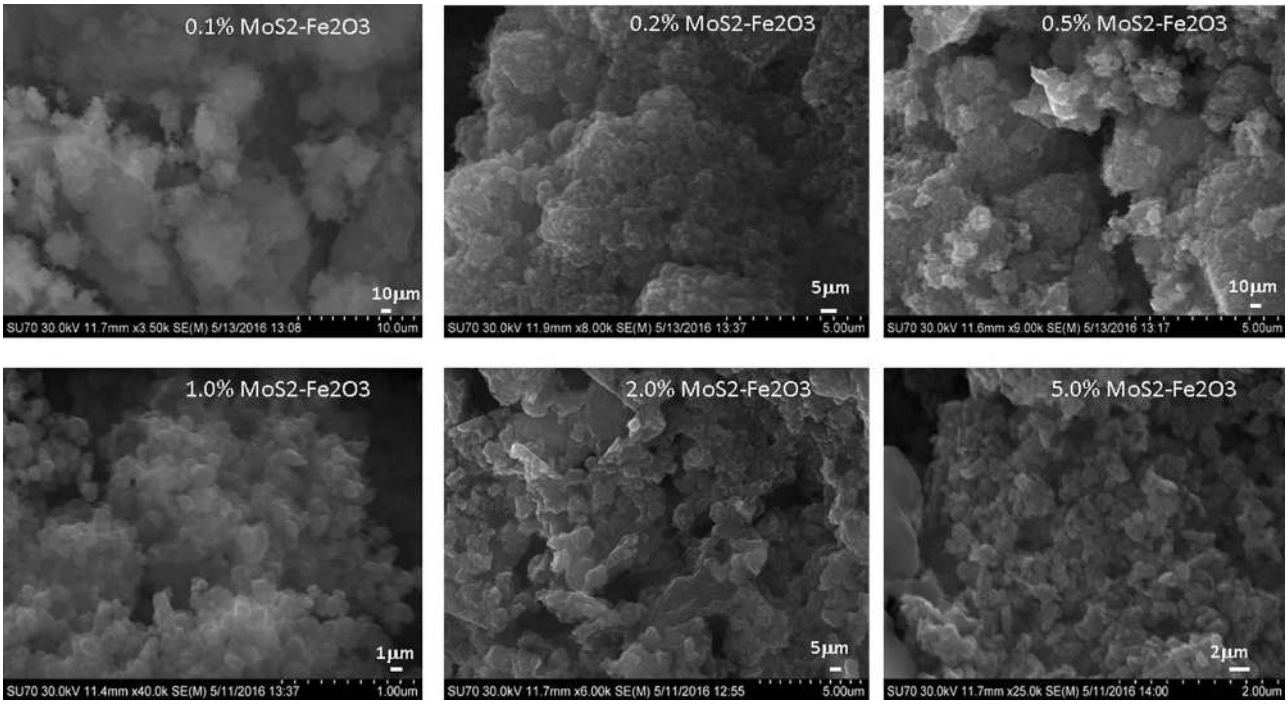

Figure 5. Scanning electron micrographs (SEM) of MoS_2 with α-hematite nanocomposite. The percentage of MoS_2 with α-hematite nanocomposite is shown in **Figure 5**.

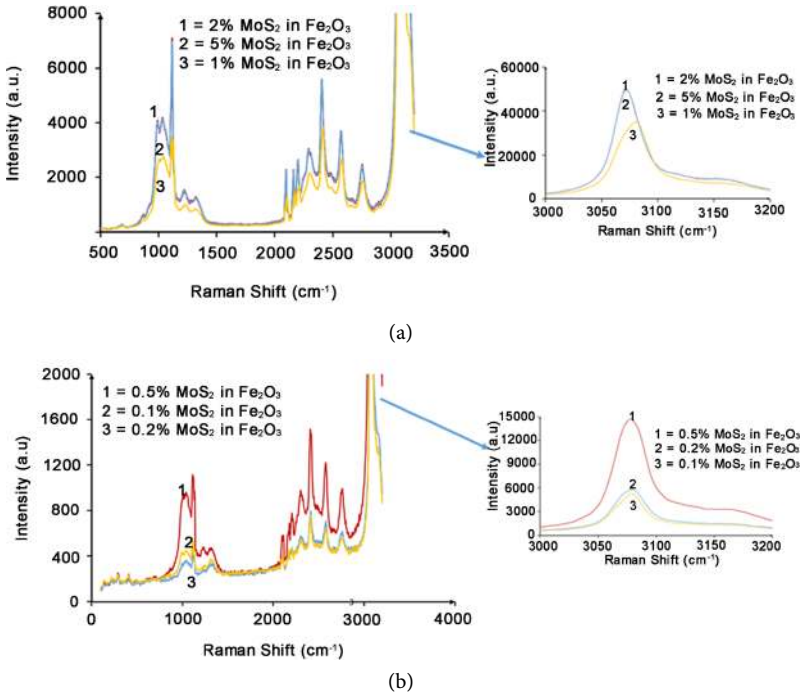

Figure 6. Raman spectra of MoS_2-α-Fe_2O_3 film sample and ITO substrate as various percentage of MoS_2 as shown in figures.

3.6. Particle Analysis

The Zetasizer Nano particle analyzer range model was used to measure the average particle size of various MoS_2-α-Fe_2O_3 samples. Initially, the MoS_2-α-Fe_2O_3

nanomaterial was dispersed in water and ultra-sonicated to have aggregated free colloidal sample. Figure 7 shows the particle size of MoS_2-α-Fe_2O_3 as a function of MoS_2 doping in α-Fe_2O_3. The average particle size in liquid sample ranges from 459 nm (0.1%) to 825 nm for (5%) do pant of MoS_2 respectively. Although these particles are small, there are few particles which are larger than 5 microns. These larger particles that can be detected through SEM measurement are a result of aggregation. The average size of particles is important for the fabrication of the electrodes from the particles. This information of nanomaterial dispersion of MoS_2-α-Fe_2O_3 can be exploited for the electrode fabrication or other applications.

3.7. Electrochemical Studies

3.7.1. Cyclic Voltammetry

The electrochemical measurements on various MoS_2-α-Fe_2O_3 electrodes were measured from electrochemical workstation (Volta lab). The electrochemical set-up was adopted similar to our earlier studies on hybrid films [45] [46]. Figure 8 shows the cyclic voltammetry (CV) of 1% MoS_2-α-Fe_2O_3 in 1M NaOH as working electrode, platinum (Pt) as counter and Ag/AgCl as reference electrode in three electrodes based electrochemical cell. The continuous increase of CV current was observed with an increase in function of scan rate. The presence of MoS_2 ions induces the electrochemical properties and 1.3 V can be seen as oxidation potential of water that is less than the Aluminum-doped from our previous studies [30].

The CV is shown in Figure 9 with application of light simulated for solar radiation. However, with the scan rate of 100 mV/sec, there was a maximum photocurrent absorbed for MoS_2-α-Fe_2O_3 film. The diffusion coefficient was

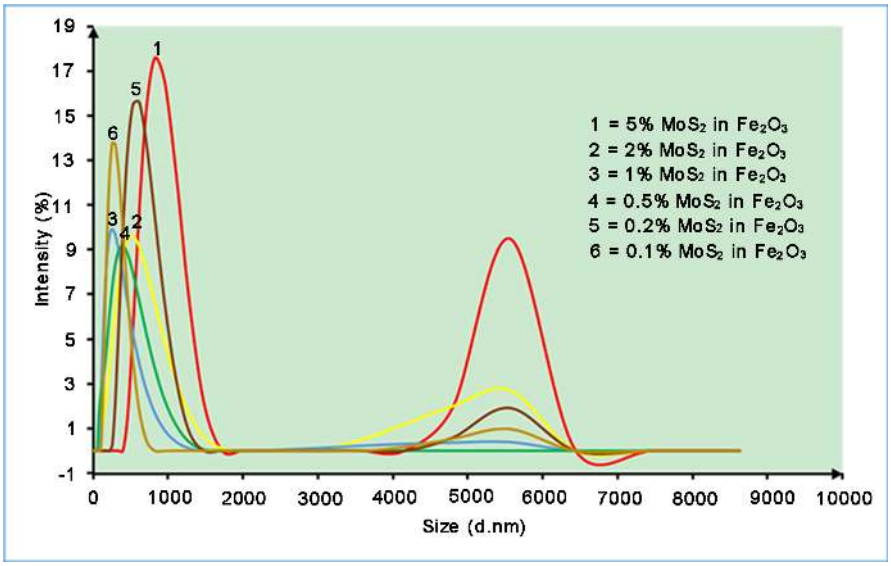

Figure 7. The particle size measurement of MoS_2-α-Fe_2O_3 nanocomposite materials as a function of MoS_2 dopant.

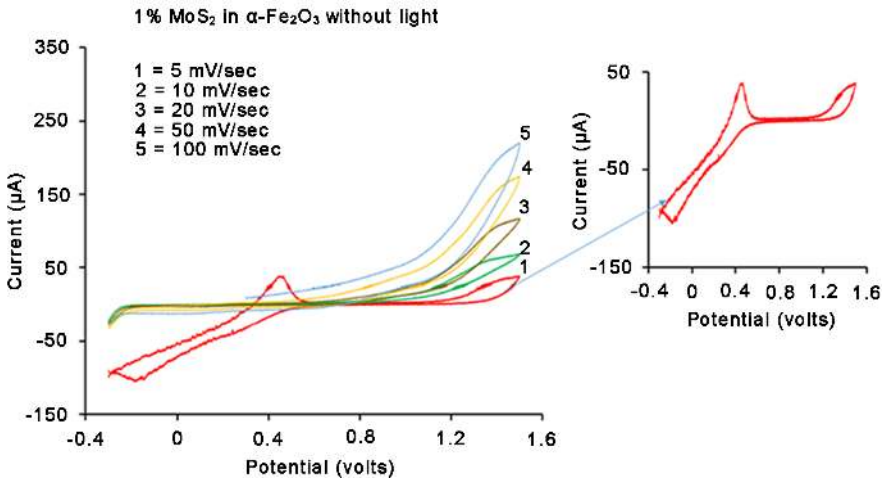

Figure 8. The cyclic voltammetry of 1% MoS_2 with Fe_2O_3 nanocomposite without light in 1 M NaOH in three electrodes where platinum as reference and Ag/AgCl as reference electrode.

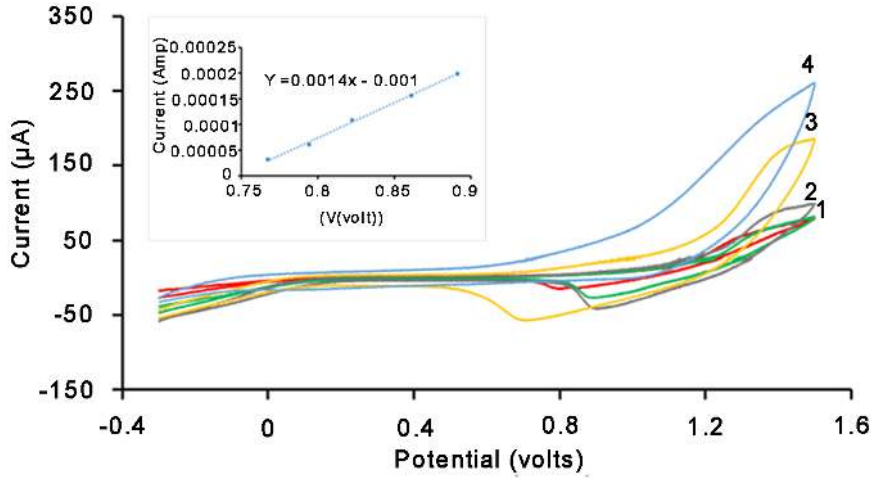

Figure 9. The cyclic voltammetry of 1% MoS_2 with Fe_2O_3 nanocomposite with light in 1 M NaOH in three electrodes where platinum as reference and Ag/AgCl as reference electrode.

calculated by using peak current for a reversible cyclic voltammetry is given by the Randles-Sevcik equation (Equation (2)).

$$I_P = \left(2.69 \times 10^5\right) n^{3/2} ACD^{1/2} v^{1/2} \tag{2}$$

where:

n = number of electrons

A = electrode area (cm^2)

C = concentration ($mole/cm^3$)

D = diffusion coefficient (cm^2/s)

v = potential scan rate (V/s)

I_p = current.

The diffusion coefficient has been estimated to be 0.24×10^{-16} cm^2/s.

3.7.2. Chronoamperometry Study

We made an attempt to deposit MoS_2-α-Fe_2O_3 film on ITO coated glass substrates uniformly using the homogenous paste obtained using acetic acid. The thickness of MoS_2-α-Fe_2O_3 was around 30 μm. **Figure 10(a)** & **Figure 10(b)** shows the chronoamperometry study of two electrodes cell consisting of MoS_2-α-Fe_2O_3 film as working and steel as counter in various concentrations (0.01 0.1, 1 M) of NaOH based electrolyte. The potential from −1000 mV to 1500 mV was applied, and the chronoamperometry photocurrent was studied. **Figure 10(a)** & **Figure 10(b)** shows the chronoamperometry photocurrent plot with $t^{-1/2}$ for oxidation and reduction processes for MoS_2-α-Fe_2O_3 film. The rise of photocurrent showed a linear relationship with $t^{-1/2}$ due to excitation of light. The current transient was different from the excitation of light. The diffusion-controlled photocurrent is calculated using Cottrell equation in Equation (3) [47] [48] [49].

$$i = \left[nFAD^{\frac{1}{2}}C \right] \Big/ \left[\pi t^{\frac{1}{2}} \right] \tag{3}$$

where:

n = the electron participating in the reaction

F = the faraday constant

A = the area of the electrode

i = the transient current

D = the diffusion coefficient

C = the concentration of the electrolyte

The D has been estimated to be 1.057×10^{-14} cm^2/sec.

3.7.3. Impedance Study

Figure 11(a) and **Figure 11(b)** show the Nyquist plot in 1 M NaOH without and with light irradiation in MoS_2-α-Fe_2O_3 film in a photoelectrochemical

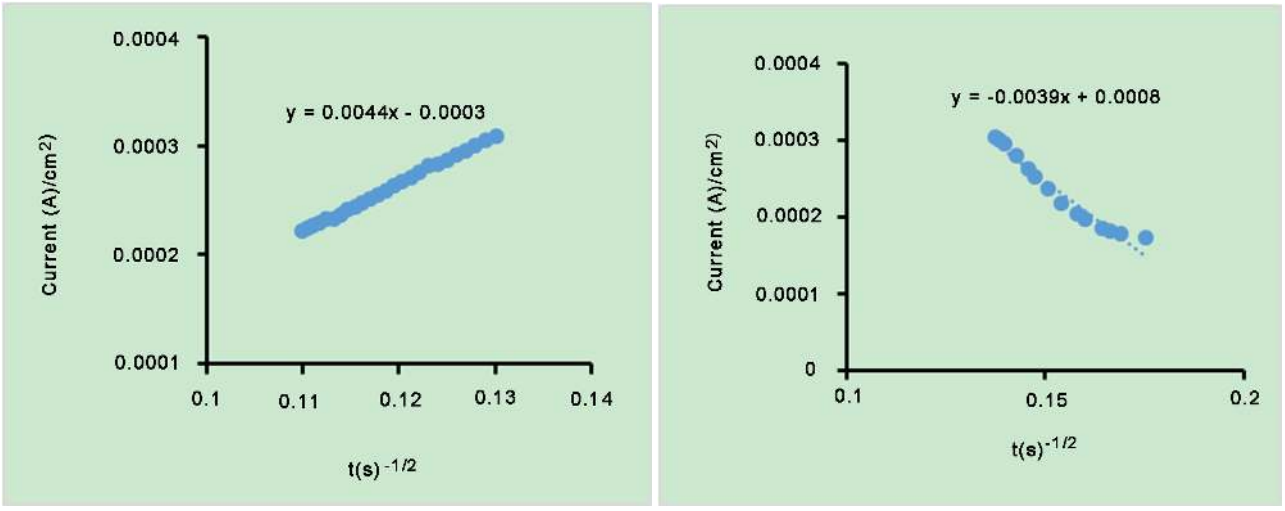

(a) (b)

Figure 10. The chronoamperometry photocurrent plot with $t(s)^{-1/2}$ for oxidation and reduction processes for MoS_2-α-Fe_2O_3 film.

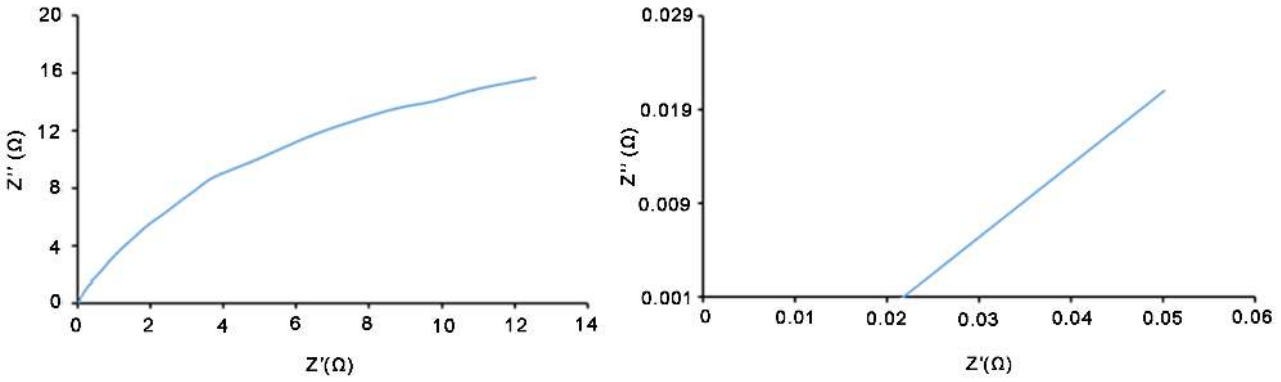

(a) (b)

Figure 11. Nyquist plot of MoS_2-α-Fe_2O_3 film in 1 M HCl in photoelectrochemical cell without (a) and with (b) light irradiation.

set-up. The change in the impedance value has been observed for real and imaginary without light irradiation as shown in **Figure 11(a)** and **Figure 11(b)**. The photocurrent is able to make process more conducting in presence of light.

3.7.4. Half Sweep Potential

Figure 12 shows the half sweep potential with and without light for both aluminum doped-α-$Fe_2O_3$and MoS_2-α-Fe_2O_3. Our previous study on aluminum doping has shown the photocurrent to be 35 μA whereas for the same type of electrode for MoS_2-α-Fe_2O_3 showed the current to be 150 μA. Schottky type current-voltage is experienced for both aluminum doped as well as MoS_2-α-Fe_2O_3 based electrode in photoelectrochemical cell.

3.8. Schematic of MoS_2-α-Fe_2O_3 Reaction Process

A schematic was drawn to understand the effect of MoS_2 with α-Fe_2O_3. The schematic of hydrogen production using MoS_2-composite α-Fe_2O_3 photocatalyst in 1 M NaOH is shown in **Figure 13**. The bandgap of MoS_2 varies from 1.2 - 1.9 eV, whereas the band gap of α-Fe_2O_3 is 2.1 eV. It was estimated the bandgap of MoS_2-composite α-Fe_2O_3 in range of 1.94 to 2.40 eV based on UV-vis measurements, which is well in the region of visible light. MoS_2 doping also increased the conductivity of the samples. The schematic in **Figure 12** shows the photogenerated electrons from conduction band of MoS_2 is transferred to conduction band (CB) of α-Fe_2O_3 whereas holes from α-Fe_2O_3 e are transferred to valence band (VB) of MoS_2. This enhances the photocatalytic activity of MoS_2 composite with α-Fe_2O_3 in MoS_2-α-Fe_2O_3 nanomaterial-based electrode.

4. Conclusions

The synthesized MoS_2-α-Fe_2O_3 observed the shift in the band gap to 2.17 eV with MoS_2 doping. There is a marked change in the band due to MoS_2 doping in α-Fe_2O_3. The increase of MoS_2 dominated the structure as marked from SEM measurements. The photocurrent can be clearly distinguishable with and without light irradiation through various electrochemical studies on MoS_2-α-Fe_2O_3

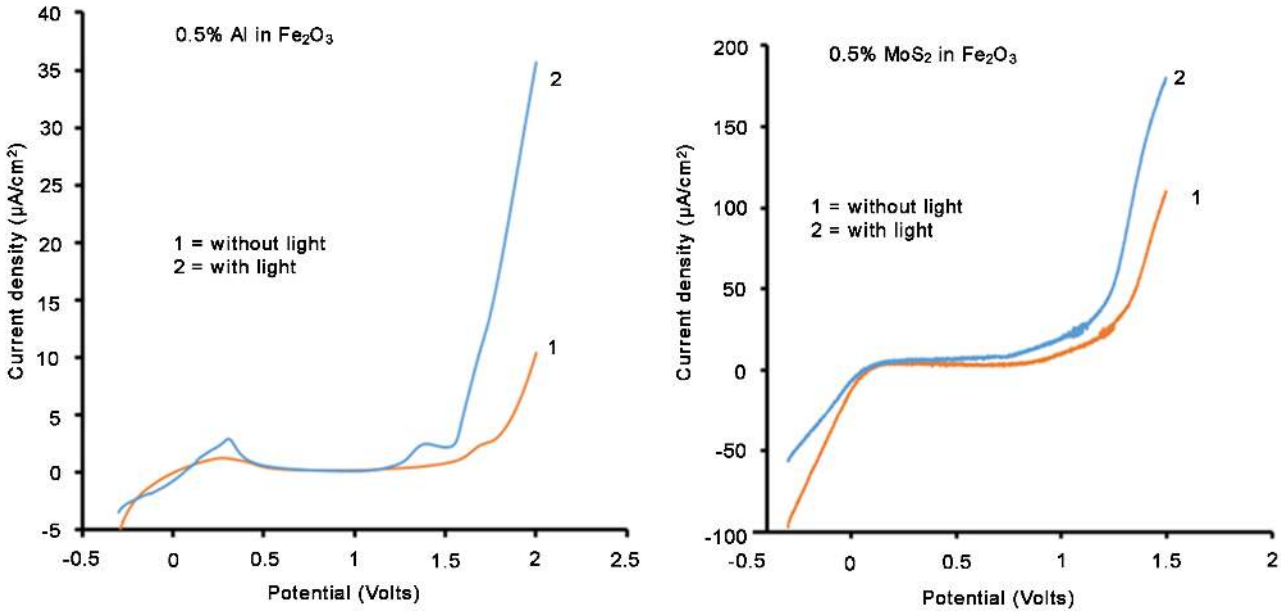

Figure 12. Half sweep potential with and without light for Aluminum doped-α-Fe_2O_3 and MoS_2-α-Fe_2O_3 film with and without light exposure.

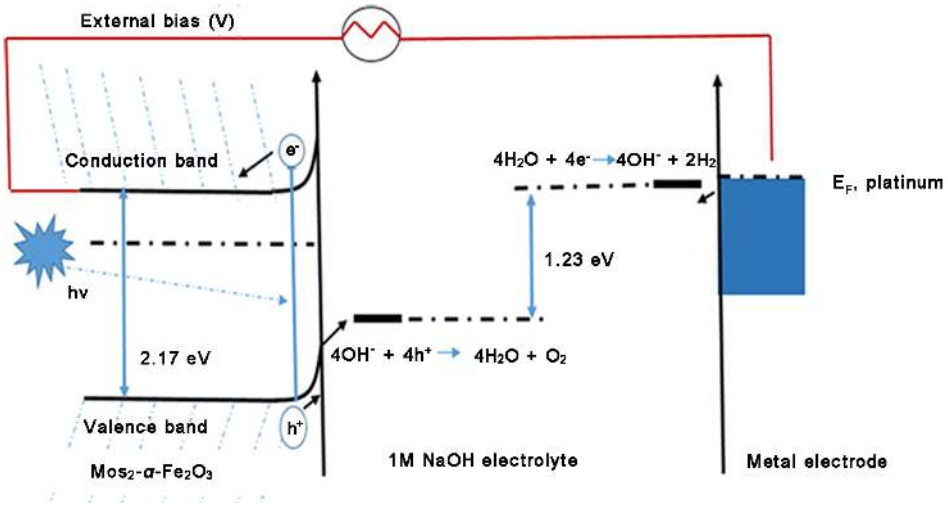

Figure 13. The schematic of hydrogen production using MoS_2-composite α-Fe_2O_3 photocatalyst in 1 M NaOH.

nanomaterial. The enhanced photocurrent is observed with MoS_2 doping in MoS_2-α-Fe_2O_3 nanomaterial. The MoS_2-α-Fe_2O_3 nanomaterial thin film has the potential to produce hydrogen using a PEC water splitting process that could have renewable energy applications. Our future work is based on the use of MoS_2-α-Fe_2O_3 as n-type in p-n photoelectrochemical studies for efficient water splitting applications.

Acknowledgements

The authors are grateful to Sina and Mike McCrory for their help in X-ray diffraction, EDS and SEM measurements.

References

[1] Wheeler, D.A., Wang, G., Ling, Y., Li, Y. and Zhang, J.Z. (2012) Nanostructured Hematite: Synthesis, Characterization, Charge Carrier Dynamics, and Photoelectrochemical Properties. *Energy & Environmental Science*, **5**, 6682-6702. https://doi.org/10.1039/c2ee00001f

[2] Li, Y., Wang, H., Xie, L., Liang, Y., Hong, G. and Dai, H. (2011) MoS_2 Nanoparticles Grown on Graphene: An Advanced Catalyst for the Hydrogen Evolution Reaction. *Journal of the American Chemical Society*, **133**, 7296-7299. https://doi.org/10.1021/ja201269b

[3] Sivula, K., Le Formal, F. and Grätzel, M. (2011) Solar Water Splitting: Progress Using Hematite (α-Fe_2O_3) Photoelectrodes. *ChemSusChem*, **4**, 432-449. https://doi.org/10.1002/cssc.201000416

[4] Hiralal, P., Saremi-Yarahmadi, S., Bayer, B.C., Wang, H., Hofmann, S., Wijayantha, K.U. and Amaratunga, G.A. (2011) Nanostructured Hematite Photoelectrochemical Electrodes Prepared by the Low Temperature Thermal Oxidation of Iron. *Solar Energy Materials and Solar Cells*, **95**, 1819-1825. https://doi.org/10.1016/j.solmat.2011.01.049

[5] Ahn, H.-J., Yoon, K.-Y., Kwak, M.-J., Lee, J.-S., Thiyagarajan, P. and Jang, J.-H. (2015) MoS_x Supported Hematite with Enhanced Photoelectrochemical Performance. *Journal of Materials Chemistry A*, **3**, 21444-21450. https://doi.org/10.1039/C5TA06743J

[6] Hisatomi, T., Kubota, J. and Domen, K. (2014) Recent Advances in Semiconductors for Photocatalytic and Photoelectrochemical Water Splitting. *Chemical Society Reviews*, **43**, 7520-7535. https://doi.org/10.1039/C3CS60378D

[7] Kim, J.Y., Magesh, G., Youn, D.H., Jang, J.-W., Kubota, J., Domen, K. and Lee, J.S. (2013) Single-Crystalline, Wormlike Hematite Photoanodes for Efficient Solar Water Splitting. *Scientific reports*, **3**, 2681. https://doi.org/10.1038/srep02681

[8] Kment, S., Hubicka, Z., Krysa, J., Sekora, D., Zlamal, M., Olejnicek, J., Cada, M., Ksirova, P., Remes, Z. and Schmuki, P. (2015) On the Improvement of PEC Activity of Hematite Thin Films Deposited by High-Power Pulsed Magnetron Sputtering Method. *Applied Catalysis B: Environmental*, **165**, 344-350. https://doi.org/10.1016/j.apcatb.2014.10.015

[9] Hisatomi, T., Dotan, H., Stefik, M., Sivula, K., Rothschild, A., Grätzel, M. and Mathews, N. (2012) Enhancement in the Performance of Ultrathin Hematite Photoanode for Water Splitting by an Oxide Underlayer. *Advanced Materials*, **24**, 2699-2702. https://doi.org/10.1002/adma.201104868

[10] Ahn, H.-J., Kwak, M.-J., Lee, J.-S., Yoon, K.-Y. and Jang, J.-H. (2014) Nanoporous Hematite Structures to Overcome Short Diffusion Lengths in Water Splitting. *Journal of Materials Chemistry A*, **2**, 19999-20003. https://doi.org/10.1039/C4TA04890C

[11] Satsangi, V.R., Kumari, S., Singh, A.P., Shrivastav, R. and Dass, S. (2008) Nanostructured Hematite for Photoelectrochemical Generation of Hydrogen. *International Journal of Hydrogen Energy*, **33**, 312-318.

[12] Du, C., Yang, X., Mayer, M.T., Hoyt, H., Xie, J., McMahon, G., Bischoping, G. and Wang, D. (2013) Hematite-Based Water Splitting with Low Turn-On Voltages. *Angewandte Chemie International Edition*, **52**, 12692-12695. https://doi.org/10.1002/anie.201306263

[13] Desai, J., Pathan, H., Min, S.-K., Jung, K.-D. and Joo, O.S. (2005) FT-IR, XPS and PEC Characterization of Spray Deposited Hematite Thin Films. *Applied Surface Science*, **252**, 1870-1875.

[14] Bassi, P.S., Wong, L.H. and Barber, J. (2014) Iron Based Photoanodes for Solar Fuel Production. *Physical Chemistry Chemical Physics*, **16**, 11834-11842. https://doi.org/10.1039/c3cp55174a

[15] Tamirat, A.G., Rick, J., Dubale, A.A., Su, W.-N. and Hwang, B.-J. (2016) Using Hematite for Photoelectrochemical Water Splitting: A Review of Current Progress and Challenges. *Nanoscale Horizons*, **1**, 243-267.

[16] Kumari, S., Tripathi, C., Singh, A.P., Chauhan, D., Shrivastav, R., Dass, S. and Satsangi, V.R. (2006) Characterization of Zn-Doped Hematite Thin Films for Photoelectrochemical Splitting of Water. *Current Science*, **91**, 1062-1073.

[17] Jorand Sartoretti, C., Alexander, B.D., Solarska, R., Rutkowska, I.A., Augustynski, J. and Cerny, R. (2005) Photoelectrochemical Oxidation of Water at Transparent Ferric Oxide Film Electrodes. *The Journal of Physical Chemistry B*, **109**, 13685-13692. https://doi.org/10.1021/jp051546g

[18] Kennedy, J.H. and Frese, K.W. (1978) Photooxidation of Water at α-Fe_2O_3 Electrodes. *Journal of the Electrochemical Society*, **125**, 709-714. https://doi.org/10.1149/1.2131532

[19] Kleiman-Shwarsctein, A., Hu, Y.-S., Forman, A.J., Stucky, G.D. and McFarland, E.W. (2008) Electrodeposition of α-Fe_2O_3 Doped with Mo or Cr as Photoanodes for Photocatalytic Water Splitting. *The Journal of Physical Chemistry C*, **112**, 15900-15907. https://doi.org/10.1021/jp803775j

[20] Kleiman-Shwarsctein, A., Huda, M.N., Walsh, A., Yan, Y., Stucky, G.D., Hu, Y.-S., Al-Jassim, M.M. and McFarland, E.W. (2009) Electrodeposited Aluminum-Doped α-Fe_2O_3 Photoelectrodes: Experiment and Theory. *Chemistry of Materials*, **22**, 510-517. https://doi.org/10.1021/cm903135j

[21] Hu, Y.-S., Kleiman-Shwarsctein, A., Forman, A.J., Hazen, D., Park, J.-N. and McFarland, E.W. (2008) Pt-Doped α-Fe_2O_3 Thin Films Active for Photoelectrochemical Water Splitting. *Chemistry of Materials*, **20**, 3803-3805. https://doi.org/10.1021/cm800144q

[22] Saremi-Yarahmadi, S., Wijayantha, K.U., Tahir, A.A. and Vaidhyanathan, B. (2009) Nanostructured α-Fe_2O_3 Electrodes for Solar Driven Water Splitting: Effect of Doping Agents on Preparation and Performance. *The Journal of Physical Chemistry C*, **113**, 4768-4778. https://doi.org/10.1021/jp808453z

[23] Kay, A., Cesar, I. and Grätzel, M. (2006) New Benchmark for Water Photooxidation by Nanostructured α-Fe_2O_3 Films. *Journal of the American Chemical Society*, **128**, 15714-15721. https://doi.org/10.1021/ja064380l

[24] Ding, Q., Meng, F., English, C.R., Cabán-Acevedo, M., Shearer, M.J., Liang, D., Daniel, A.S., Hamers, R.J. and Jin, S. (2014) Efficient Photoelectrochemical Hydrogen Generation using Heterostructures of Si and Chemically Exfoliated Metallic MoS_2. *Journal of the American Chemical Society*, **136**, 8504-8507.

[25] Yoon, K.-Y., Lee, J.-S., Kim, K., Bak, C.H., Kim, S.-I., Kim, J.-B. and Jang, J.-H. (2014) Hematite-Based Photoelectrochemical Water Splitting Supported by Inverse Opal Structures of Graphene. *ACS Applied Materials & Interfaces*, **6**, 22634-22639. https://doi.org/10.1021/am506721a

[26] Meng, F., Li, J., Cushing, S.K., Bright, J., Zhi, M., Rowley, J.D., Hong, Z., Manivannan, A., Bristow, A.D. and Wu, N. (2013) Photocatalytic Water Oxidation by Hematite/Reduced Graphene Oxide Composites. *ACS Catalysis*, **3**, 746-751. https://doi.org/10.1021/cs300740e

[27] Liu, Y., Yu, Y.-X. and Zhang, W.-D. (2013) MoS_2/CdS Heterojunction with High Photoelectrochemical Activity for H_2 Evolution under Visible Light: The Role of

MoS_2. *The Journal of Physical Chemistry C*, **117**, 12949-12957. https://doi.org/10.1021/jp4009652

[28] Alrobei, H. (2017) A-Hematite-Molybdenum Disulfide and Polyhexylthiophene (RRPHTh)-Nanodiamond (ND) Electrodes for Photoelectrochemical Applications. 3*rd International Conference on Smart Materials* & *Structures*, Orlando.

[29] Alrobei, H., Kumar, A. and Ram, M.K. (2015) Aluminum Doped *α*-Hematite for Photoelectrochemical Applications. Research Day 2015 at USF College of Engineering, Tampa.

[30] Alrobei, H., Kumar, A. and Ram, M.K. (2017) Aluminum—A-Hematite Thin Films for Photoelectrochemical Applications. Surface Review and Letters (Communicated).

[31] Chen, Z., Cummins, D., Reinecke, B.N., Clark, E., Sunkara, M.K. and Jaramillo, T.F. (2011) Core-Shell MoO_3-MoS_2 Nanowires for Hydrogen Evolution: A Functional Design for Electrocatalytic Materials. *Nano Letters*, **11**, 4168-4175. https://doi.org/10.1021/nl2020476

[32] Bonde, J., Moses, P.G., Jaramillo, T.F., Nørskov, J.K. and Chorkendorff, I. (2009) Hydrogen Evolution on Nano-Particulate Transition Metal Sulfides. *Faraday Discussions*, **140**, 219-231. https://doi.org/10.1039/B803857K

[33] Kibsgaard, J., Chen, Z., Reinecke, B.N. and Jaramillo, T.F. (2012) Engineering the Surface Structure of MoS_2 to Preferentially Expose Active Edge Sites for Electrocatalysis. *Nature Materials*, **11**, 963-969. https://doi.org/10.1038/nmat3439

[34] Thurston, T. and Wilcoxon, J. (1999) Photooxidation of Organic Chemicals Catalyzed by Nanoscale MoS_2. *The Journal of Physical Chemistry B*, **103**, 11-17. https://doi.org/10.1021/jp982337h

[35] Han, S., Hu, L., Liang, Z., Wageh, S., Al-Ghamdi, A.A., Chen, Y. and Fang, X. (2014) One-Step Hydrothermal Synthesis of 2D Hexagonal Nanoplates of *α*-Fe_2O_3/Graphene Composites with Enhanced Photocatalytic Activity. *Advanced Functional Materials*, **24**, 5719-5727. https://doi.org/10.1002/adfm.201401279

[36] Alrobei, H., Kumar, A. and Ram, M.K. (2016) Doped A-Hematite with Molybdenum Sulfides MoS_2 for Photoelectrochemical Applications. 9*th Annual College of Engineering Research Day*, Tampa.

[37] Chemelewski, W.D., Mabayoje, O., Tang, D., Rettie, A.J. and Mullins, C.B. (2016) Bandgap Engineering of Fe_2O_3 with Cr-Application to Photoelectrochemical Oxidation. *Physical Chemistry Chemical Physics*, **18**, 1644-1648. https://doi.org/10.1039/C5CP05154A

[38] Sun, S., Sun, M., Kong, Y., Fang, Y. and Yao, Y. (2016) MoS_2 and Graphene as Dual, Cocatalysts for Enhanced Visible Light Photocatalytic Activity of Fe_2O_3. *Journal of Sol-Gel Science and Technology*, **80**, 719-727.

[39] Srivastava, S. (2012) Synthesis and Characterization of Iron Oxide Nanoparticle from $FeCl_3$ by Using Polyvinyl Alcohol. *International Journal of Physical and Social Sciences*, **2**, 161-184.

[40] Woo, K., Lee, H.J., Ahn, J.-P. and Park, Y.S. (2003) Sol-Gel Mediated Synthesis of Fe_2O_3 Nanorods. *Advanced Materials*, **15**, 1761-1764. https://doi.org/10.1002/adma.200305561

[41] Gao, D., Si, M., Li, J., Zhang, J., Zhang, Z., Yang, Z. and Xue, D. (2013) Ferromagnetism in Freestanding MoS_2 Nanosheets. *Nanoscale Research Letters*, **8**, 129. https://doi.org/10.1186/1556-276X-8-129

[42] Zhang, Y., Chen, P., Wen, F., Meng, Y., Yuan, B. and Wang, H. (2016) Synthesis of S-Rich Flower-Like Fe_2O_3-MoS_2 for Cr (VI) Removal. *Separation Science and Technology*, **51**, 1779-1786.

[43] Yang, X., Sun, H., Zhang, L., Zhao, L., Lian, J. and Jiang, Q. (2016) High Efficient Photo-Fenton Catalyst of α-Fe_2O_3/MoS_2 Hierarchical Nanoheterostructures: Reutilization for Supercapacitors. *Scientific Reports*, **6**, Article No. 31591. https://doi.org/10.1038/srep31591

[44] Ye, L., Wang, D. and Chen, S. (2016) Fabrication and Enhanced Photoelectrochemical Performance of MoS_2/S-Doped G-C_3N_4 Heterojunction Film. *ACS Applied Materials & Interfaces*, **8**, 5280-5289. https://doi.org/10.1021/acsami.5b11326

[45] Giambrone, N., McCrory, M., Kumar, A. and Ram, M.K. (2016) Comparative Photoelectrochemical Studies of Ragioregular Polyhexylthiophene with Microdiamond, Nanodiamond and Hexagonal Boron Nitride Hybrid Films. *Thin Solid Films*, **615**, 226-232.

[46] Basnayaka, P.A., Villalba, P., Ram, M.K., Stefanakos, L. and Kumar, A. (2013) Photovoltaic Properties of Multi Walled Carbon Nanotubes-Poly (3-Octathiophene) Conducting Polymer Blends Structures. In: *MRS Proceedings*, Cambridge University Press, Cambridge, 139-144.

[47] Bard, A.J. and Faulkner, L.R. (1980) Electrochemical Methods. Wiley, New York.

[48] Ram, M.K., Maccioni, E. and Nicolini, C. (1997) The Electrochromic Response of Polyaniline and Its Copolymeric Systems. *Thin Solid Films*, **303**, 27-33.

[49] Ram, M., Sundaresan, N. and Malhotra, B. (1994) Performance of Electrochromic Cells of Polyaniline in Polymeric Electrolytes. *Journal of Materials Science Letters*, **13**, 1490-1493. https://doi.org/10.1007/BF00419144